



HAL
open science

Ceilometer inversion method using water-vapor correction from co-located microwave radiometer for aerosol retrievals

Andres E. Bedoya-Velásquez, Marcos Herreras-Giralda, Roberto Román, Matthias Wiegner, Sidonie Lefebvre, Carlos Toledano, Thierry Huet, Romain Ceolato

► To cite this version:

Andres E. Bedoya-Velásquez, Marcos Herreras-Giralda, Roberto Román, Matthias Wiegner, Sidonie Lefebvre, et al.. Ceilometer inversion method using water-vapor correction from co-located microwave radiometer for aerosol retrievals. *Atmospheric Research*, 2021, 250, pp.105379. 10.1016/j.atmosres.2020.105379 . hal-02865809v2

HAL Id: hal-02865809

<https://hal.science/hal-02865809v2>

Submitted on 12 Jan 2021

HAL is a multi-disciplinary open access archive for the deposit and dissemination of scientific research documents, whether they are published or not. The documents may come from teaching and research institutions in France or abroad, or from public or private research centers.

L'archive ouverte pluridisciplinaire **HAL**, est destinée au dépôt et à la diffusion de documents scientifiques de niveau recherche, publiés ou non, émanant des établissements d'enseignement et de recherche français ou étrangers, des laboratoires publics ou privés.

Ceilometer inversion method using water-vapor correction from co-located microwave radiometer for aerosol retrievals

A. E. Bedoya-Velásquez^a, M. Herreras-Giralda^{b,c}, R. Román^d, M. Wiegner^e,
S. Lefebvre^f, C. Toledano^d, T. Huet^a, R. Ceolato^a

^a*The French Aeospace Lab, ONERA, Toulouse, France*

^b*GRASP-SAS, Remote sensing developments, Université des Sciences et Technologies de Lille, Villeneuve d'Ascq, France*

^c*Laboratoire d'Optique Atmosphérique, Université des Sciences et Technologies de Lille, Villeneuve d'Ascq, France*

^d*Grupo de óptica atmosférica, Universidad de Valladolid, Valladolid, Spain*

^e*Meteorologisches Institut, Ludwig-Maximilians-Universität, Theresienstraße 37, 80333 München, Germany*

^f*The French Aeospace Lab, ONERA, Palaiseau, France*

Abstract

Recent ceilometer models are more sensitive to aerosols, which is increasing the interest in these instruments to retrieve aerosol optical and microphysical properties. In this paper, a new methodology is proposed to retrieve aerosol vertical extinction and backscatter profiles from a Vaisala ceilometer CL51 model. This methodology is based in two parts: first, a signal pre-processing with a suppression of the dark current and background noises, and a correction of the water vapor absorption using near-real-time temperature and absolute humidity (AH) profiles from a co-located Microwave radiometer (MWR). The measured dark current shows a height-dependence from 11 km agl to the end of the profile. From the water vapor correction, it was seen that the raw ceilometer signal overestimates the water vapour corrected one, mainly below 1 km agl. Second part is based on an iterative Klett-based algorithm making use of AERONET (AErosol RObotic NETwork) AOD (Aerosol Optical Depth) and ceilometer profiles as inputs to retrieve the extinction and backscatter profiles. The sensitivity of the aerosol retrievals to the use of modelled temperature and absolute humidity from HYSPLIT to correct water vapor absorption, instead of MWR measurements, is studied. The absolute errors found in temperature and AH profiles

leads to errors in the pre-processed range corrected signals up to 9%, and then in particle backscatter (β_p) and particle extinction (α_p) coefficients up to 2.2 % and 25 %, respectively.

Keywords: Aerosol inversion, Vaisala ceilometer, microwave radiometry, ceilometer data pre-processing

1 Introduction

Atmospheric aerosols play a crucial role in atmospheric dynamics and the energy balance of the Earth. The main impact of the aerosols related-interactions are: (i) the aerosol-radiation interaction (ARI), affecting the radiative fluxes of the Earth by absorbing and scattering solar and thermal radiation, and (ii) aerosol-cloud interaction (ACI) which are mainly associated to the modification of cloud properties and precipitation caused by aerosols ([1]). During the last decades, different active and passive remote sensors in synergistic operation have become a powerful strategy for the better determination of the atmospheric aerosol properties (optical and microphysical). Previous works have shown that synergy between active remote sensors as lidar systems (light detection and ranging) and passive remote sensors, e.g. sunphotometers or microwave radiometer (MWR), allows to obtain advanced and vertically resolved aerosol properties ([2, 3, 4, 5]) and to study phenomena like aerosol hygroscopic growth ([6]) and the aerosol vertical dynamics using as proxy the planetary boundary layer (PBL) height ([7]). The main drawbacks of these synergies are the cost of having the instrumentation operating together and also that most of the instruments are semi-automatic, which means that qualified human operation is frequently needed.

Ceilometers are low power single-wavelength lidar-based instruments which operate automatically, unattended and continuously. These instruments are commonly used for cloud base height determination and PBL studies, but recently, ceilometers have become an useful alternative for aerosol studies such as typical robust lidar instruments. These systems have been widely spread along the world with more than 1000 ceilometers installed over Europe, Asia and America. Currently, the COST Action ES1303 TOPROF (TOwards operational ground based PROFiling with ceilometers, doppler lidars and microwave radiometers for improving weather forecasts) has dedicated part of their interests on working in a better characterization of the ceilometer

31 products and related uncertainties, and also E-PROFILE, a program of EU-
32 METNET (EUropean METeorological services NETwork), is focused on the
33 harmonization of ceilometer measurements and data provision across Eu-
34 rope, meaning that the interest in quantitative aerosol products from these
35 instruments is increasing. In the last decade, ceilometers started to be used
36 for long term studies of phenomena less investigated with remote sensors
37 like aerosol hygroscopic growth ([8]), to improve the forecasting models for
38 example to predict fog events ([9]), to retrieve profiles of aerosol properties
39 ([10, 11, 12, 13] and to characterize them ([14] and [15]).

40
41 CHM15k ceilometer model (Lufft manufacturer) is widely used for aerosol
42 inversion, mainly because it operates with a similar configuration as the com-
43 mercial lidar systems, therefore the quality of the signals have been deeply
44 studied and their capabilities are well known [12, 13]. Other ceilometers used
45 for the same end are the CL31 and CL51 models (Vaisala Inc.), but as it has
46 been shown in [16], depending of the firmware and other features, Vaisala
47 ceilometers present some drawbacks such as non-expected signal shapes and
48 high electronic noises. In [17] is presented a new type of correction that im-
49 proves the signal shape, named dark signal removal, making a substitution
50 of the dark current measurements. In addition, as the emission line of the
51 Vaisala CL-51 ceilometer is centered around 910 nm, water vapor absorp-
52 tion plays a critical role affecting the quality of the signal. [18] describes a
53 methodology to make a water vapor correction of the signal using modelled
54 water vapor absorption cross section and radiosondes for retrieving aerosol
55 properties. After considering all this pre-processing, it is possible to use the
56 ceilometer signal for aerosol retrieval using traditional methods such as the
57 Klett’s algorithm ([19, 12]).

58
59 The main objective of this work is to present a new methodology, based
60 on a modified Klett algorithm [12], to retrieve optical aerosol properties from
61 Vaisala CL51 ceilometers. To this end, a data pre-processing is required, in-
62 cluding the suppression of the dark current noise (DCN), height-dependant
63 background (BG) noises, and water vapor correction in near-real time by
64 using a co-located microwave radiometer (MWR). The methodology allows
65 to determine the error propagation when modelled atmospheric profiles are
66 used for aerosol inversion products instead of using co-located measurements.

67
68 The manuscript is organized as follows. The site, instrumentation and

69 data used are presented in Section 2, while Section 3 explain the applied
70 methodology in terms of the signal pre-processing. Section 4 describes the
71 Klett method to retrieve the aerosol profiles, and Section 5 shows the un-
72 certainty in the retrievals caused by the use of water vapor derived from
73 modelled radiosoundings instead of MWR data. Finally, Section 6 summa-
74 rizes the main conclusions.

75 **2. Site, Instrumentation and data availability**

76 *2.1. ONERA site*

77 ONERA, the French Aerospace Lab, is a research institute located in
78 Toulouse, Occitanie, in the southern part of France (N: 43°34'12", E: 128°24").
79 The mission of the Optictronics department (DOTA) is to conduct studies
80 and research in Optronics. These studies are conducted primarily for the ben-
81 efit of the fields of Aeronautics, Space and Defence, but also for other fields
82 such as security, environment, astronomy and medical imaging. MELOPEE
83 Lab is a light-scattering lidar laboratory dedicated to the development of
84 active remote-sensing instrument for light-scattering investigations. For this
85 work, a ceilometer and a ground-based microwaver radiometer located on
86 roof-top of the building were used for this experiment. Toulouse is a re-
87 gion with a humid subtropical climate dominated by Autan wind, which is a
88 south-easterly wind from the Mediterranean. Due to the Garone river that di-
89 vides the city between east and west crossing it from south to north, Toulouse
90 presents rather high relative humidity (around 80%) almost all over the year.
91 The seasonal behaviour drives to have hot summers and cold winters.

92 *2.2. Vaisala CL51 ceilometer*

93 A CL51 Vaisala ceilometer, located at the ONERA site, have been used
94 in this work. This is an active remote sensor that operates continuously
95 (24/7) emitting pulsed laser radiation towards the atmosphere centered at
96 910 ± 10 nm. The backscattered radiation by the atmosphere is collected
97 by a telescope in coaxial configuration, reducing the overlap height. Unless
98 the ceilometer is a new instrument with less than a year to be installed
99 and the fact that manufacturer provided an overlap information that assures
100 full-overlap after 50m, we have considered our products above 250 m agl be-
101 cause this work is not focused in the near-field measurements. The detection
102 system is based on an APD detector. The backscattered signal from the
103 atmosphere is measured with spatial and temporal resolutions up to 10 m

104 and 15 s respectively. More technical information can be found in [16]. The
 105 spectral range of the emitted and received light by the instrument is affected
 106 by atmospheric water vapor absorption, which has a direct impact on the
 107 recorded attenuated backscatter profile, which is the main product of the
 108 instrument.

109

110 Considering a single scattering approximation and assuming that lidar
 111 constant (K) and overlap ($O(R)$) are well known, the ceilometer retrieved
 112 signal based on the elastic lidar equation can be written as follows:

$$\frac{RCS(R)}{K_0 O(R)} = U(R) = \beta(R) \exp \left[-2 \int_0^R \alpha(r) dr \right] \quad (1)$$

113 where $RCS(R)$ is the range corrected signal (the recorded signal divided
 114 by the square of range); K_0 is a constant that involves system characteris-
 115 tics (optics and electronics); $O(R)$ is the overlap function referring to the
 116 geometrical probability of fully signal collection as a function of height; β is
 117 the backscatter coefficient. The double pathway atmospheric transmittance
 118 is defined as $T^2(R) = \exp \left[-2 \int_0^R \alpha(r) dr \right]$ where α is the atmospheric ex-
 119 tinction coefficient. In a general formulation, β and α takes into account the
 120 contribution of the particles and molecules in the atmosphere [20, 19].

121 The $U(R)$ term is the main product retrieved from ceilometers, but in
 122 practice this coefficient cannot be always determined because K_0 and $O(R)$
 123 parameters are unknown most of the time. Due to this elastic lidar formu-
 124 lation, the wavelength dependency is omitted from the equations. The ana-
 125 lytical solution of the Eq.1 can be obtained by using Klett-Fernald method
 126 ([20, 19]) assuming a constant extintion-to-backscatter ratio, also known as
 127 lidar ratio (LR). Other atmospheric parameters are involved in the solution
 128 of the lidar equation, but those will be discussed in further sections. The
 129 data used in this work were measured continuously from October to Novem-
 130 ber 2019 with temporal resolution about 36 s/profile and vertical resolution
 131 of 10 m (from 10 m to 15400 km agl). The instrument records 2400 measures
 132 per day of RCS profiles, but it also provides cloud base height, and other
 133 metadata.

134 2.3. RPG-HATPRO MWR

135 A ground-based microwave radiometer (RPG-HATPRO, Radiometer physics
 136 GmbH) is co-located to the mentioned ceilometer. MWR is considered as a

137 passive remote sensor that performs measures unattended of the brightness
138 temperatures of oxygen and water vapor in the atmosphere. The oxygen is
139 measured in the K-band (51-58 GHz) and the water vapor in the V-band
140 from 22 to 31 GHz with a radiometric resolution between 0.3 and 0.4 rms
141 errors at 1.0 s integration time.

142

143 A previously trained neural network algorithm ([21]) is used to retrieve
144 temperature and relative humidity (RH) and absolute humidity (AH) pro-
145 files. The temperature and RH profiles are provided at 92 height bins with
146 variable vertical resolution and covering the first 10 km of the atmosphere.
147 Temperature and RH profiles performance (accuracy and precision) has been
148 studied in previous studies using radiosondes as references and finding that
149 the temperature accuracy and precision is up to $1 \pm$ K and close to 6 ± 8
150 % for RH under cloud-free conditions [22]; this pointed out the potential of
151 these systems to retrieve atmospheric variables. Regarding the data avail-
152 ability for this study, the MWR provides up to 600 temperature, relative
153 humidity and absolute humidity profiles per day with temporal resolution
154 up to 2 min/profile. Temperature profiles had a composite format that com-
155 bined the high spatial resolution of the atmospheric boundary layer profiles
156 product with the standard temperature profiles.

157 2.4. CIMEL sun/sky photometer

158 A sun/sky photometer CIMEL CE318-N (Cimel Electronique S.A.S.)([23])
159 is operating since 2013 at the south-east part of Toulouse (43.57 N, 1.37 E, at
160 160 m asl), up to 8 km away from the ceilometer in straight line. This instru-
161 ment provides automatic measurements of sun and sky radiation at several
162 wavelengths (340, 380, 440, 500, 675, 870, 940, 1020 and 1640 nm).These
163 measurements are processed by AERONET in order to derive the optical
164 and microphysical aerosol properties integrated in column [23]. The main
165 AERONET product is the spectral aerosol optical depth (AOD_λ). In ad-
166 dition, the channel of 940 nm is used for retrieving the total column water
167 vapor (or precipitable water vapor). AERONET also uses AOD_λ and almucantar
168 sky radiance measurements to retrieve and provide additional aerosol
169 properties including volume size distribution, complex refraction index, and
170 single scattering albedo at various wavelengths ([24, 25, 26]).In this work,
171 the AERONET AOD data used is the AERONET level 1.5 (cloud-screened)
172 from AERONET version 3 ([27]), with an uncertainty lower than ± 0.01 for
173 the wavelengths larger than 440 nm and below 0.02 for shorter wavelengths.

174 *2.5. Hysplit GDAS meteorological data base*

175 As a result of the computer analysis and forecast calculation performed
176 at the centers for Environmental prediction (NCEP), it is possible to use an
177 operational system so called Global Assimilation Data System (GDAS) for
178 running the Hybrid Single Particle Lagrangian Integrated Trajectory Model
179 (HYSPLIT)([28]). One of the HYSPLIT modules allows to retrieve modelled
180 radiosondes with different spatial and temporal resolutions. In this work, we
181 have retrieved HYSPLIT profiles of temperature, relative humidity and pres-
182 sure for ONERA location with spatial resolution of 0.5 and 3 h of temporal
183 resolution. The total database of radiosoundings used for this study is 488
184 profiles (October and November 2019) from 0 to 10 km.

185 **3. Signal pre-processing**

186 The methodology developed in this paper involves the following 2 stages
187 (Fig.1): (i) the signal pre-processing: contain dark current (DC), background
188 (BG) and water vapor correction by using real co-located atmospheric mea-
189 surements and (ii) refers to the semi-automatic Klett algorithm.

190 *3.1. Dark current correction*

191 First, a ceilometer data pre-processing is performed. For signal noise cor-
192 rection, two types of signal are taken into account. The first one is linked
193 with the electrical noise of the detectors which is so called dark current noise
194 (DCN). In this work, DCN measurements were carried out under day-time
195 and night-time conditions using the termination hood accessory delivered
196 with the ceilometer shipping for covering the instrument to avoid external
197 light contamination, however some reflections in the near field are still re-
198 mained (below 50m). The DCN was regularly measured twice per week dur-
199 ing two weeks, taking samples of 30 minutes at day and night time. During
200 the analyzed period (October-November 2019) DCN does not show a high
201 variability between days, therefore we focused our attention on the day-time
202 and night-time analysis. As example, Fig.2a presents the day-time(gray line)
203 and night-time (black line) mean DCN profiles measured from 0.010 km to
204 15.4 km agl for the 11th October 2019. The bias between the profiles (not
205 shown) in the first kilometers after full overlap (from 0.80m to 1km agl) is
206 close to zero, but it increased rapidly with height: bias from 1 to 2 km agl
207 increased from 2.5 to 5.0 a.u, from 2 to 6 km agl increased from 5 to 25 a.u
208 and above this height the bias reached up values above 300 a.u. The shape

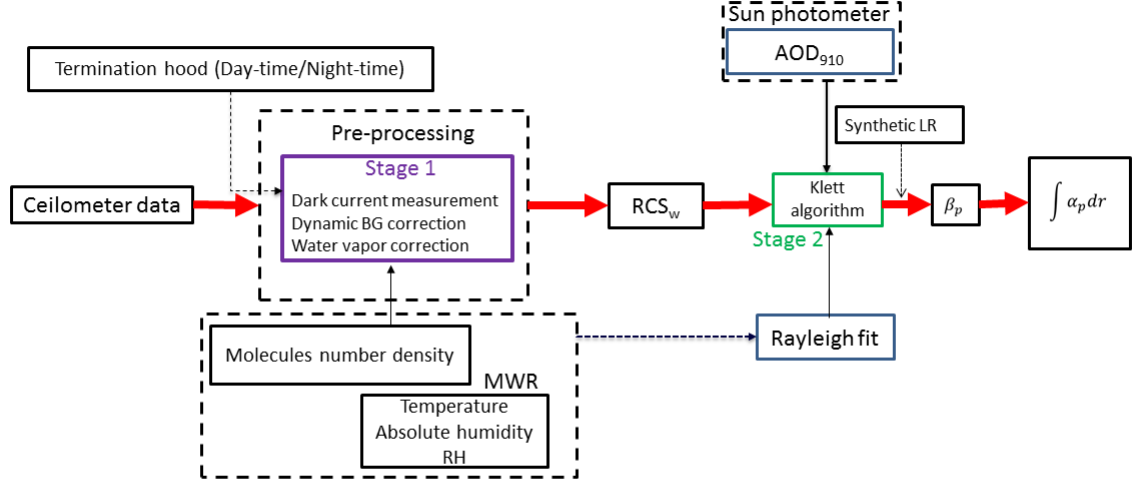


Figure 1: Block diagram of the methodology

209 of the DCN signal is relatively well balance between negative and positive
 210 values around zero until 9 km agl (see Fig.2b), but above this height the
 211 signal is fluctuating strongly describing a S-shape. From 9 to 11 km agl pos-
 212 itive curve can be observed, then the signal decrease from 11 to 14 km agl
 213 describing a negative curve for finally increase again from 14 km to the end
 214 of the profile. To focus the attention in the shape of the DCN, we plotted
 215 the smoothed the DCN in Fig.2b, observing that the noise is quite oscillating
 216 around zero for daytime (due to the light contamination) than night-time,
 217 but the shape remains. Once the DCN is characterized, it must be directly
 218 subtracted from the range corrected ceilometer raw data.

219 According to [16] results, this behavior can be expected for Vaisala ceilome-
 220 ters, however this analysis let us evidence the impact that DCN suppression
 221 will have on the RCS_{raw} signal. The signal-to-noise ratio (SNR) of this in-
 222 strument decrease above 4 km agl, which was checked for the raw signal
 223 (not shown) and range corrected (see Fig.2c). The RCS_{raw} signal shown in

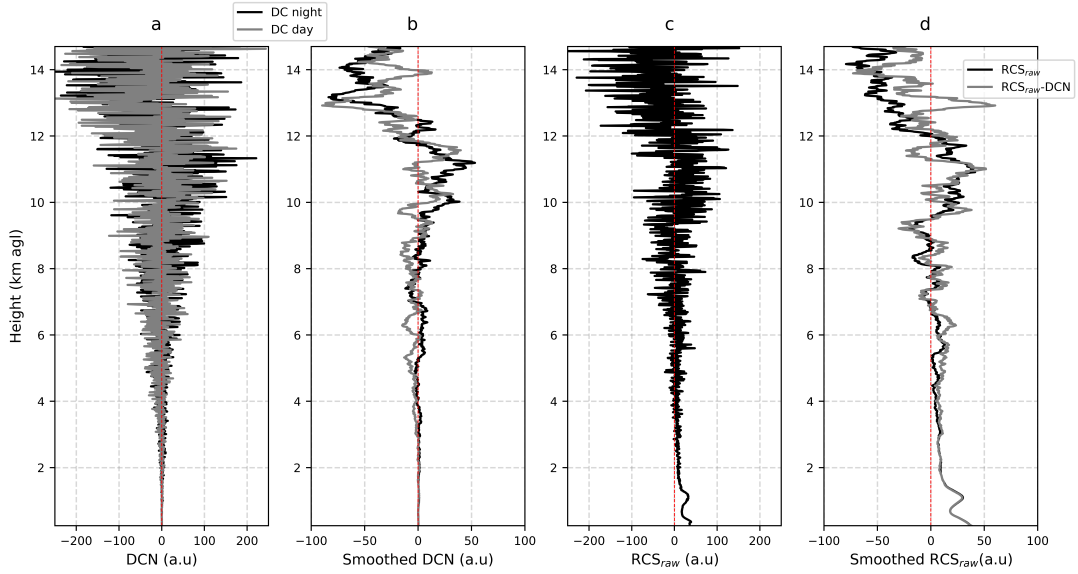


Figure 2: Example measurements corresponding to 11th October 2019. Here, the ceilometer DCN correction is shown. a) The DCN measurements are presented in black: night-time and gray: day-time; b) the smoothed DCN smoothed profiles (for the sake of clarity, but not considered in the calculations); c) the RCS_{raw} signal 1h-averaged, and d) the RCS_{raw} DCN corrected (smoothed)

224 Fig.2b was 1h-averaged in order to minimize spatial fluctuations. Testing
 225 with the RCS_{raw} , it was possible to determine that the RCS_{raw} and DCN
 226 keep the same shape from 7km agl until the maximum range of the profile,
 227 which give us the possibility to minimize these fluctuations with continu-
 228 ous DCN measurements, and also to define the regions for suppressing the
 229 environment-light noise, so called background (BG).

230

231 Figure 2c is illustrating the RCS_{raw} shape before any DCN subtraction.
 232 The DCN signals shown in Fig.2b and the corrected ones presented in Fig.2d
 233 were smoothed by applying a filter (i.e. spatial-averaging) just for centering
 234 the attention on the main shape of the RCS_{raw} without all of these elec-
 235 trical fluctuations shown in Fig.2ac, but these smoothed profiles were never
 236 involved in the calculations. The first difference between black and gray pro-
 237 files shown in Fig.2d is the minimization of the S-shape fluctuation and sec-
 238 ondly the reduction/suppression of some near-range electronic fluctuations.
 239 After DCN correction, it can be noticed that the signal is noise cleaned up

240 to 4 km agl, and the S-shape oscillation of the RCS_{raw} has been reduced.
241 This S-shape of the Vaisala ceilometer signal is related to the opto-electronic
242 system noises, but this analysis is beyond of the scope in this work.

243 *3.2. Background noise*

244 The second noise evaluated during the data pre-processing is the envi-
245 ronmental light contamination of the ceilometer signal, which plays a role as
246 a bias to the signal and it is well-known as background (BG) noise. This
247 calculation was performed after DCN correction to have a signal with a sig-
248 nificant reduction in the electronic fluctuations (i.e. minimization of the last
249 kilometers oscillation). The BG is a constant value commonly consider as
250 the mean value in the last kilometers of the lidar signals (i.e. 1 kilometer or
251 more), but only if the signal present a constant noise. In our case, the sig-
252 nals were not so well behaved, unless that, we have reduced the oscillations
253 considerably by suppressing DCN. As we shown in Fig.3, the BG presented
254 a height-dependency from 7 to 15.4 km agl, therefore the following ranges
255 of the profile were evaluated: BG1 (7-9 km agl), BG2 (9-11 km agl), BG3
256 (11-13 km agl) and BG4 (13-15.4km agl). One positive aspect observed on
257 this height-dependency is that BG noise at each range presented a normal
258 distribution (not shown here). Therefore, each range-dependent BG mean
259 calculated for each profile is a good candidate to suppress the BG noise.
260 Finally, we use the BG value that improved the dynamic range of the pro-
261 files (i.e. allows us to have positive signal in a far range), meaning that we
262 systematically analyse each profile, then we performed the DCN correction
263 and finally chose the best BG as it shown in Fig.3. Summarizing up, this
264 procedure will enhance the probability of having good RCS profile to invert
265 until 6 km agl, and it also improves the signal-to-noise ratio (SNR) in the
266 medium/far range. The fact that ceilometers present a low SNR above 7 km
267 agl suggest that only big events such as clouds and big aerosol plumes can
268 be properly detected.

269 The signal retrieved from the Vaisala ceilometers presents a challenge
270 to be pre-processed in order to retrieve aerosol optical properties. One of
271 the main challenges is addressed in [16], where it was showed that most of
272 Vaisala systems have a positive or negative signal distortion associated to
273 electronic noise fluctuations. The correction of this fluctuation is tackled by
274 suppressing cosmetic offsets ([16]) or dark corrections ([17]). In this work,
275 the DCN measurement and also the search of the best BG value assure that

276 signal noise level and shape is improved. The corrected signal is defined in
277 the manuscript as follows

$$RCS^*(R) = RCS_{raw} - [DCN + BG] \quad (2)$$

278 where RCS_{raw} is the raw range corrected signal, DCN is a 30 min av-
279 eraged profile and BG is the mean value that fulfilled the criteria already
280 explained.

281
282 In Fig.3 is presented the whole scheme of the signal pre-processing, show-
283 ing that good BG selection is not a trivial process for ceilometers. In the
284 example case showed in the top of the panel of Fig.3ad, it is performed the
285 pre-processing on 11th October 2019 at 7 UTC and in the bottom of the panel
286 (Fig.3e-h) at 10 UTC. In black dots it is represented the signal spatially- av-
287 eraged each 500m together with the standard deviation. This representation
288 has two aims, in one hand to evidence the shape of the RSC_{raw} and how it
289 improves after the DCN suppression for different profiles. It can be noticed
290 after this correction that the oscillation of the averaged points is substan-
291 tially reduced in the far and near range. On the other hand, we can notice in
292 Fig.3b-f that there is a remaining oscillating noise above 7 km agl, therefore is
293 imperative to evaluate the height-dependency of BG noise. The Fig.3 shows
294 that the ceilometer BG noise is changing from one measurement to another,
295 therefore the application of a systematic BG correction must be considered to
296 each profile separately and checking which BG value improves the dynamic
297 range. From the example case at 7 UTC, we use the BG4, while at 10 UTC
298 the BG2 was the one that improved the signal. With this procedure, we are
299 increasing the amount of signal available to invert.

300 3.3. Water vapor correction

301 As mentioned before, one of the CL51 drawbacks is the impact of the wa-
302 ter vapor absorption on the laser emission line Previous works have demon-
303 strated that this effect can be minimized. The water vapor correction method
304 used in this paper is based on the one proposed by [18]. To perform this cor-
305 rection, absolute humidity and temperature profiles are used as input. In
306 this paper, those profiles were measured from co-located MWR each 2 min
307 from 0 to 10 km agl. These profiles were interpolated to the ceilometer ver-
308 tical resolution. Regarding the temporal coincidence of the measurements,
309 the temporal resolution of the ceilometer was degraded to the MWR.

310

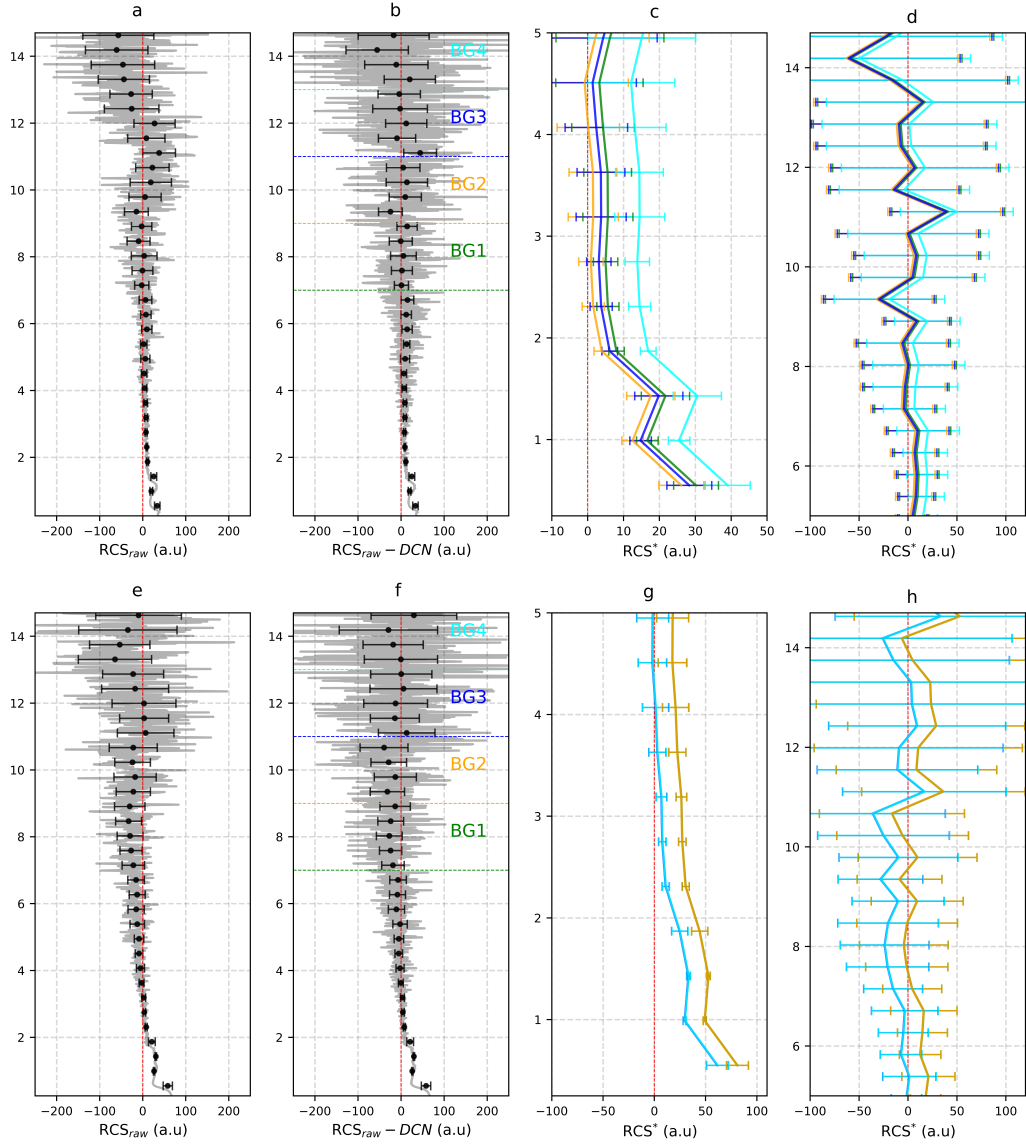


Figure 3: The figure presents the noise pre-processing applied to obtain the $RCS_* = RCS_{raw} - (DC + BG)$. The measurements were taken on 11th October 2019. In the upper part are presented the results at 7 UTC and the bottom at 10 UTC. The four BG ranges are shown. In green line is related to the correction for BG1, orange to BG2, blue to BG3 and cyan to BG4. The standard deviation calculated corresponds to 500m-average in order to gain visibility at each step of the signal pre-processing.

311 For the water vapor correction it is necessary to rewrite the transmittance
 312 term presented in Sec.2.2, splitting the transmittance term into the contri-
 313 butions of the molecules, particles and water vapor (T_m^2 , T_p^2 , T_w^2). In this
 314 work, the transmittance term for molecules is calculated by using Rayleigh
 315 theory fed with atmospheric measurements (temperature and RH) from the
 316 MWR. Transmittance from particles can be determined as a result of the
 317 crosschecking procedure during the Klett inversion explained below. T_w^2 can
 318 be defined as:

$$T_w^2 = \exp \left[-2 \int_0^R \alpha(r)_w dr \right] \quad (3)$$

319 Where $\alpha(r)_w = \sigma(r)_w N(r)_w$, with $N(r)_w$ the water vapor number concen-
 320 tration and $\sigma(r)_w$ is the absorption cross section at the emitted wavelength.
 321 The $N(r)_w$ will be calculated from atmospheric measurements of absolute hu-
 322 midity profiles like $N(r)_w = 7.25 \times 10^{22} \text{ AH } R_w$, where $R_w = 0.462 \text{ Jg}^{-1} \text{ K}^{-1}$.
 323 $\sigma(r)_w$ is calculated following the results presented on [18] for the absorp-
 324 tion cross section simulated profiles. In this context, we consider a Gaussian
 325 shape of the ceilometer emission spectrum centered at 910 nm with $\Delta\lambda = 3.5$
 326 nm ([18]). As water vapor decrease with height, the Eq.3 is solved for the
 327 first 10 km of the atmosphere, but results are only shown until 3 km agl. The
 328 water vapor corrected profile is named hereafter as $RCS_w = RCS^*(R)/T_w^2$.

329
 330 Figure 4 shows an example case where the water vapor correction is ap-
 331 plied following the explained procedure. The atmospheric transmittance due
 332 to water vapor molecules is calculated using the profiles of temperature and
 333 AH from MWR, and from them calculate the n_w . In the example case shown
 334 in Fig.4b (red line), it is possible to evaluate the bias between RCS^* and
 335 RCS_w , meaning that ceilometer signal tends to be overestimated if water
 336 vapor correction is not applied (Fig.4b, gray line). The larger differences
 337 between water vapor corrected and no-corrected profiles are within the first
 338 1.5 km agl mainly because i) tropospheric water vapor molecules are more
 339 abundant at these altitudes, and ii) the MWR spatial resolution is better
 340 until 2 km agl. This increase of the overestimation is seen on the bias plot
 341 (Fig.4c), reaching almost 4 (a.u). The bias profile is highly noisy above 1.8
 342 km agl which is caused by the increasing of the RCS^* noise already discussed.

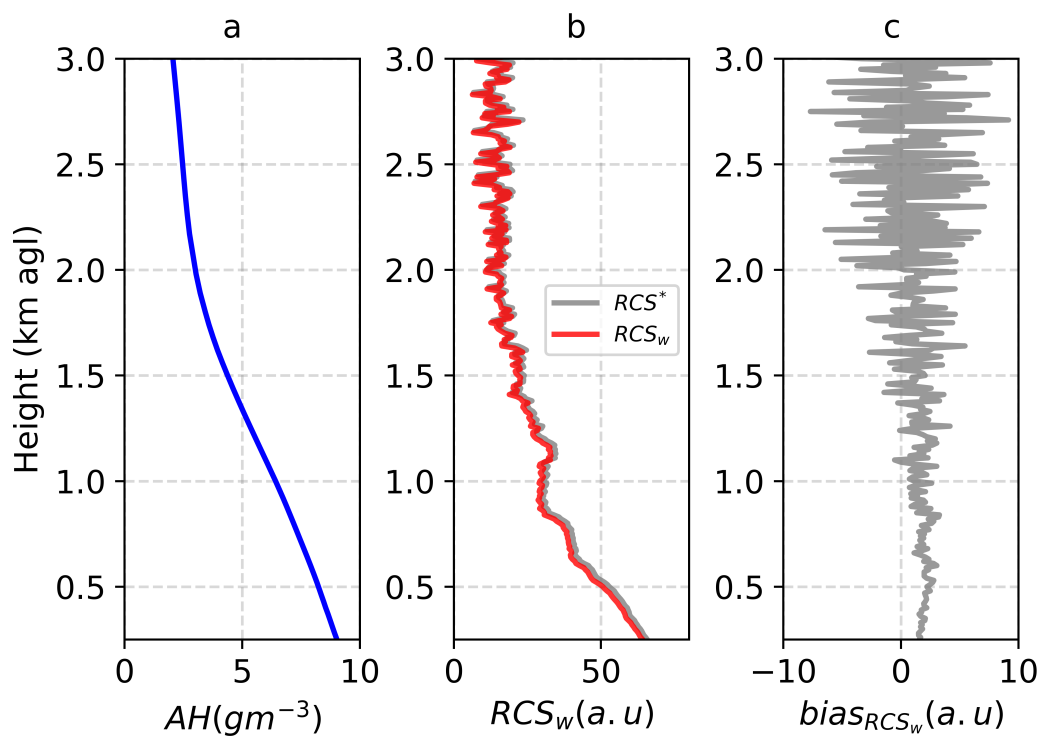


Figure 4: Water vapor correction corresponding to 11th October 2019 at 06:00 UTC. a) Blue line represents the AH profile, b) RCS_w with/without water vapor correction, red and gray line respectively are shown, and c) is the bias between RCS^* and RCS_w

343 4. Retrieval of aerosol profiles

344 Ceilometer inversions have been successfully proved in Vaisala ceilometers
345 in previous works ([17]; [18]). However one of the main challenges remain
346 in the use of ancillary information from models for correcting the signal and
347 then invert it. In this work, we propose an approach to tackle this problem by
348 combining co-located atmospheric profiles measured next to the ceilometer
349 and then applying a modified methodology of the semi-automatic lidar Klett
350 inversion proposed in [12]. The aerosol retrieval method has been divided in
351 3-step process as follows:

352

- 353 • Signal smoothing (Step 1): First the signal is noise-cleaned applying
354 a 1h average to the analyzed profiles. Then, in order to remove big
355 peaks that remained from electronic noise, a spatial filter (40 m moving
356 average filter) is applied. The aim of doing this filtering is to preserve
357 the main shape of the RCS_w with noise peak reduction.

- 358 • Rayleigh fit (Step 2): The Rayleigh fit procedure has been done by
359 normalizing the signals, β_m and RCS_w , in order to have comparable
360 magnitudes. After this normalization, it is possible to check automat-
361 ically the region where both signals have similar slopes by means of a
362 linear fitting between 2 to 5 km agl. This altitude range is pre-set as
363 an input to the algorithm in order to apply the slope's method, start-
364 ing from 2 km agl; however, in turbulent days (where the Atmospheric
365 Boundary Layer(ABL) is too high), the presence of aerosol may remain
366 at those altitudes, for that reason, we consider a range until 5 km agl,
367 assuring that the slopes will be checked for different atmospheric vol-
368 umes (each 60m) until the fulfillment of the criteria. The criteria to
369 consider that both slopes are close enough is based on the R-squared
370 is the correlation coefficient (the Goodness-of-Fit of the linear regres-
371 sion), then when $r^2 > 0.7$ between normalized β_m and RCS_w , and the
372 percentual relative error between the slopes is below 0.2, the Rayleigh
373 zone is identified. Once that a layer containing the Rayleigh informa-
374 tion has been found, just one reference point inside of it has to be
375 selected. The iterative methodology to select this Rayleigh reference
376 point is described below

- 377 • Backward Klett inversion (Step 3).

378 The aerosol retrieval starts from the following lidar equation

$$RCS_w(R) = C\beta(R)T_m^2T_p^2 \quad (4)$$

379 Then the backward Klett equation can be expressed as follows,

$$\beta_p = \frac{A_1(R)}{A_2(R)} - \beta_m(R) \quad (5)$$

380 where

$$A_1(R) = RCS_w(R) \exp \left[2 \int_r^{r_{ref}} (LR_p - LR_m)\beta_m dr \right] \quad (6)$$

381 and

$$A_2(R) = \frac{RCS_w(R)}{\beta(r_{ref})_m + \beta(r_{ref})_p} + 2 \int_r^{r_{ref}} LR(r)_p A_1(r) dr \quad (7)$$

382 where β_m is determined from Rayleigh theory using measured atmo-
 383 spheric profiles as inputs and the well-known molecular lidar ratio
 384 (LR_m) from theory. The other terms like particle lidar ratio (LR_p),
 385 and the reference height (r_{ref}) are calculated during the different steps
 386 involved in the modified [12] algorithm to Vaisala ceilometer.

387 An iterative Klett inversion process is performed for 240 values of LR
 388 ranging from 35 to 150 Sr each 0.5 sr, and for all possible height refer-
 389 ence points inside Rayleigh zone found above, in order to retrieve β_p
 390 and α_p . The goal with this iterative process is to run Klett until find
 391 a combination of LR and reference Rayleigh height that makes com-
 392 parable the integrated α_p profile with the interpolated AOD_{910} from
 393 sun photometer at the closest UTC time. The retrievals are consid-
 394 ered as successful when the difference between integrated α_p profile
 395 and AOD_{910} is lower than 0.001.

396 The results are shown in Fig.5 for the case of 11th October 2019 at ON-
 397 ERA site (occitanie Toulouse). The molecular profile (black dotted line in
 398 Fig.5a) is calculated using Rayleigh theory fed with temperature and RH pro-
 399 files from MWR. The cases presented here had a normalization range from

400 1.5 to 5 km, assuring a region where Rayleigh and RCS_w slopes are compa-
401 rable. In Fig.5a the Rayleigh zone is detected from 1.8 to 3.5 km agl, and
402 particularly in this example case a relative slope error of 0.05 with $r^2 = 0.9$
403 was found. The aim in the determination of the Rayleigh zone is to find the
404 right altitude of reference to perform the backward Klett inversion, and as we
405 see in Fig.5, due to the oscillations that remain in the RCS_w , the algorithm
406 may found a valid reference point in the far ranges within the zone selected
407 (i.e. above 3 km agl as it is shown in the figure). For that reason α_p profiles
408 are showing some variability in the proximity to the reference point (up to
409 0.006km^{-1}).

410

411 In order to assure the full overlap, it is used 250 m agl as the minimum
412 height during the Klett inversion. The example case shown here presents the
413 evolution of the inversions since early morning until afternoon. The dynamic
414 of the atmosphere started with the aerosol relatively compressed below the
415 ABL (below 0.8 km agl) due to the lack of solar radiation, but after 10 UTC
416 the layers started to mix along the atmospheric column showing two aerosol
417 accumulations, from 0.4 to 0.5 km agl and from 1.0 to 1.2 km agl. According
418 to AERONET, along the day, we had the presence of mixed aerosols between
419 urban and dust particles over Toulouse, predominating the coarse mode in
420 the size distribution reaching $0.019 \mu \text{m}^3 / \mu \text{m}^2$. The iterative Klett proce-
421 dure for having β_p profiles was performed by following the methodology, and
422 then α_p profiles were obtained as it is shown in Fig.5b. During the morning,
423 α_p was up to 0.03 km^{-1} in the first atmospheric layers (from 0.2 to 0.5 km
424 agl), and then from 10 to 15 UTC α_p reached up 0.05 km^{-1} below the first
425 0.5 km agl. $\alpha_p = 0.03 \text{ km}^{-1}$ for the pronounced aerosol peaks from 12 to 15
426 UTC.

427

428 One of the pursued parameters on lidar inversion is the LR , in our case,
429 over Toulouse area there is no previous information about this parameter,
430 therefore as one of the main goals for the application of a semi-automatic
431 Klett is to have in the near future a robust data base that will help us to un-
432 derstand better the aerosol behaviour over the region and also to have more
433 tools for retrieving aerosol optical properties. Table1 presents the LR ob-
434 tained from Klett inversion, reporting an increasing LR along the day ranging
435 from 58.1 to 99.0 sr, with a positive correlation with the AOD increase. In the
436 early morning, the LR values are comparable with those reported in [12] and
437 [17] for dust aerosols up to 60 Sr, but after 10 UTC the LR values obtained

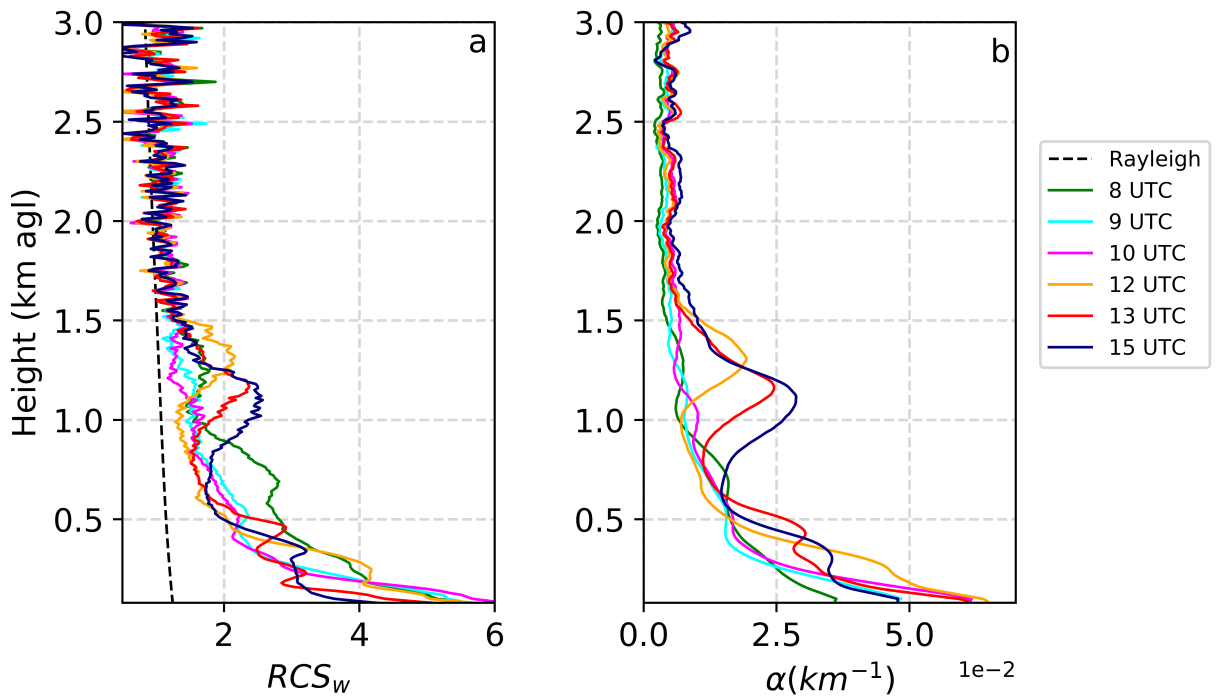


Figure 5: Example case of Klett inversion performed on 11th October 2019 for the time-frames that sun photometer has *LR* data availability. The AOD_{910} was interpolated from AERONET data at the same UTC time of the 1h-averaged RCS_w . The black dotted line in a) refers to the Rayleigh fit profile and in colors are presented in a) the RCS_w profiles used as input for the retrieval, while in b) is represented the α_p resulting from the inversion

438 here increased up to 99 sr. In most of the studies, the LR is imposed for the
 439 klett calculation because of the previous knowledge of the aerosol type, but
 440 in our case LR is obtained from the continuous AOD cross-checking during
 441 the algorithm iterations, giving us the possibility to explore a wide range of
 442 LR values that are related with different aerosol types.
 443

Table 1: Klett inversions on 11th October 2019.

UTC	Klett AOD	Klett LR (sr)
8	0.039	72.2
9	0.045	58.1
10	0.052	68.7
12	0.059	83.6
13	0.060	99.0
15	0.061	87.9

444 The larger values found for LR with Klett inversion might be associated
 445 to the presence of the mixed aerosol (e.g. polluted dust), the physical sep-
 446 aration between the sun photometer and the ceilometer, and also due to
 447 instrumental parameters that increase the uncertainties (e.g lidar constant).
 448 The inversions left two open paths for future works, from a technical sight
 449 will be the calculation of the ceilometer calibration constant along the sea-
 450 sons to considering different scenarios, and the design of the field campaigns
 451 for co-located measurements between ground base lidars and the ceilometer
 452 in order to inter-compare inversion products and improve the overlap infor-
 453 mation of the instrument. From a scientific point of view, we are studying
 454 the sensibility of the algorithm applied on synthetic lidar data and vaisala
 455 ceilometer signals in order to study the error propagation linked with the
 456 Rayleigh reference and LR values obtained along the iterations, and their
 457 impact over aerosol properties retrieved.

458 5. Errors from water vapor uncertainties

459 The methodology applied to retrieve aerosol profiles from vaisala CL51
 460 ceilometer needs the a signal deep noise pre-processing and water vapor cor-
 461 rection as we have shown in this work. Here, we have used atmospheric vari-
 462 ables from the co-located MWR to improve the results, however, the water

463 vapor correction in many stations with CL51 ceilometer is performed by tak-
 464 ing atmospheric information from models, thus an extra uncertainty is added
 465 to the RCS and then propagated to the products retrieved. For that reason,
 466 we dedicate this section to quantify the errors when modelled inputs are con-
 467 sidered instead of measured ones. The first part of this section is devoted to
 468 quantify the errors between atmospheric profiles calculated from HYSPLIT
 469 model instead of those measured with the MWR. In order to statistically
 470 characterize the errors between the model and MWR, we use the mean root
 471 mean square error (RMSE), and the mean bias error (MBE). These statistical
 472 quantities were calculated at each altitude in order to evaluate how far are
 473 the modelled data from the measured ones. The second part of this section
 474 is focused on the error quantification and its impact over the RCS_w , β_p and
 475 α_p under both scenarios, assuming modelled data and measured ones. For
 476 doing that, the percentual relative error has been used (RE), where MWR
 477 quantities are considered as the reference.

478 5.1. HYSPLIT vs MWR data

479 In order to characterize the inversion calculation, a 2-step error estima-
 480 tion procedure is proposed (see Fig.1). In the first step, it was used a 2
 481 months database (October-November 2019) from atmospheric measurements
 482 of temperature and AH from MWR, and modelled radiosondes retrieved us-
 483 ing the GDAS meteorological database from HYSPLIT model. The aim is
 484 to estimate the root mean square error (RMSE) and mean bias error (MBE)
 485 between temperature, AH and $N(r)_w$ profiles assuming MWR as the refer-
 486 ence, evaluating the error between model and MWR atmospheric data.

487
 488 Figure 6 presents the result of the two-months error comparison be-
 489 tween HYSPLIT modelled radiosondes retrieved at ONERA location using
 490 the GDAS meteorological database and the MWR profiles. The data were
 491 chosen assuring coincidence of the temporal and spatial resolutions between
 492 soundings and MWR profiles from 0 to 10 km agl. For the analysis, 488
 493 coincident cases were found. Temperature and AH, the main atmospheric
 494 variables involved in the pre-processing and inversion, were evaluated. N_w
 495 was also analyzed but the RMSE and MBE errors were relatively lower and
 496 highly dependant of the temperature and AH errors. Figure 6a,b shows in
 497 red line the temperature profiles of RMSE and MBE calculations, pointing
 498 out that below 2 km agl the RMSE reach the lowest values (lower than 4 °C),

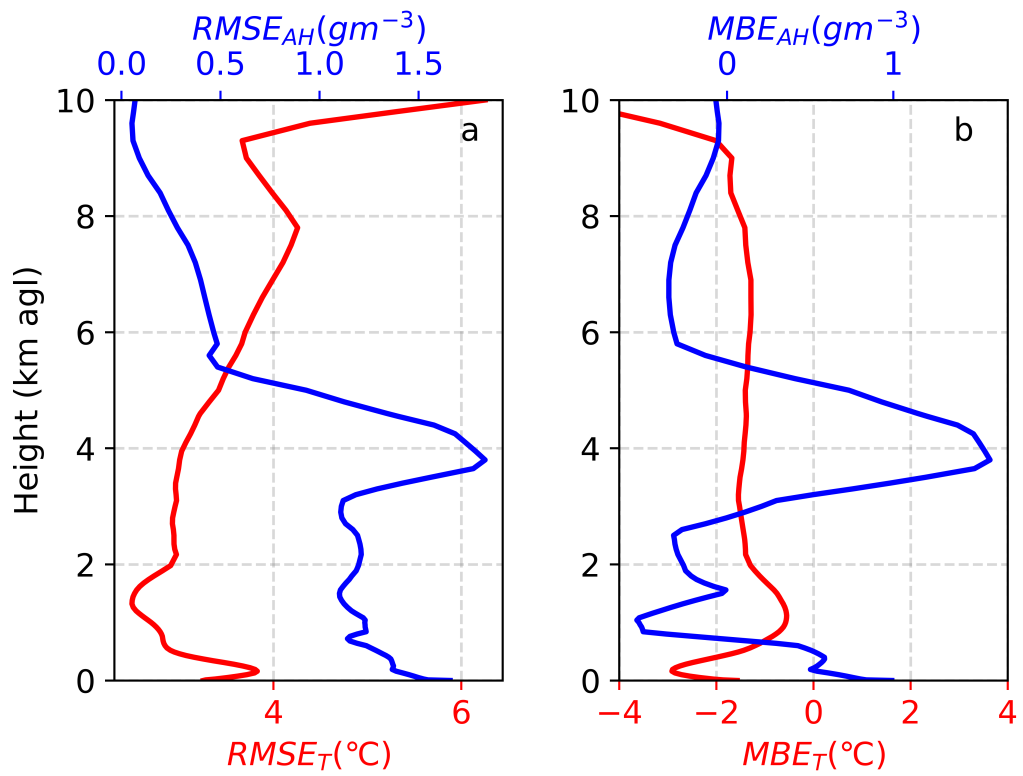


Figure 6: It is presented the error calculation in terms of RMSE and MBE, panel a) and b) respectively. For both panels, red line refers to temperature and blue line to AH.

499 but after that altitude the RMSE increase monotonically until 6 °C. There-
 500 fore assuming the MWR as the reference, the results indicate that modelled
 501 radiosondes can be far from the MWR measurements at least 4 °C in the
 502 crucial zone for ceilometer profiles. The Fig.6b shows that temperature re-
 503 trieved profiles from HYSPLIT are always sub-estimating the MWR ones,
 504 being critical around the first hundred meters agl. For AH profiles (blue
 505 lines, Fig.6a,b), the RMSE shows values below 1.5 gm⁻³ for the whole pro-
 506 file, however between 3.7 to 5.7 km agl, the RMSE presented a peak, which
 507 might be associated to the atmospheric region where the number of water
 508 vapor molecules decrease with height drastically as it was also seen in [17].
 509 The MBE of the AH is quite variable, the ranges that overestimate the profile
 510 are from 0 to 200 m and 3 km to 5.8 km agl and the sub estimation ranges
 511 are from 1 km to 2.3 km and from 5.8 km to the end.

512 5.2. Uncertainty propagation on aerosol profiles

513 The second part of the error calculation is performed just to six par-
 514 ticular cases where lidar inversion was applied. In the last section, it was
 515 seen the performance of the atmospheric variables between measured and
 516 modelled data, but here we centered our attention in determining the error
 517 propagation in terms of the percentual relative error (RE) for temperature,
 518 AH, RCS_w , β_p and α_p in order to evaluate the error propagation during inver-
 519 sion process considering modelled data instead of atmospheric measurements.

520
 521 In Fig.7 are presented the errors of the input measurements used for re-
 522 trieving β_p and α_p applying the Klett inversion already discussed. In Fig.7a
 523 is reported the percentual RE between temperature and AH profiles consid-
 524 ering MWR as reference, from there it can be seen that RE in temperature
 525 (red line) are higher in the first 800 m agl (up to 5 %), but then, the RE do
 526 not surpasses 1 %. Meanwhile, AH presented higher RE. AH relative errors
 527 (blue line) below 2 km agl were lower than 20 %, but above 2 km agl the
 528 errors can reach 100 % faster. The absolute errors on N_w at using the model
 529 or the MWR data are really lower, practically negligible (not shown here).

530
 531 Figure7b shows the RE on the RCS_w profile for the same example case
 532 presented in Sec.4. Therefore, the results of having up to 1 % RE in tem-
 533 perature and close to 20 % in AH are causing an increase in the RCS_w RE
 534 up to 30 % below 2 km agl, and above this height the absolute error increase
 535 drastically reaching up more than 100 % above 3.5 km agl. The evaluation

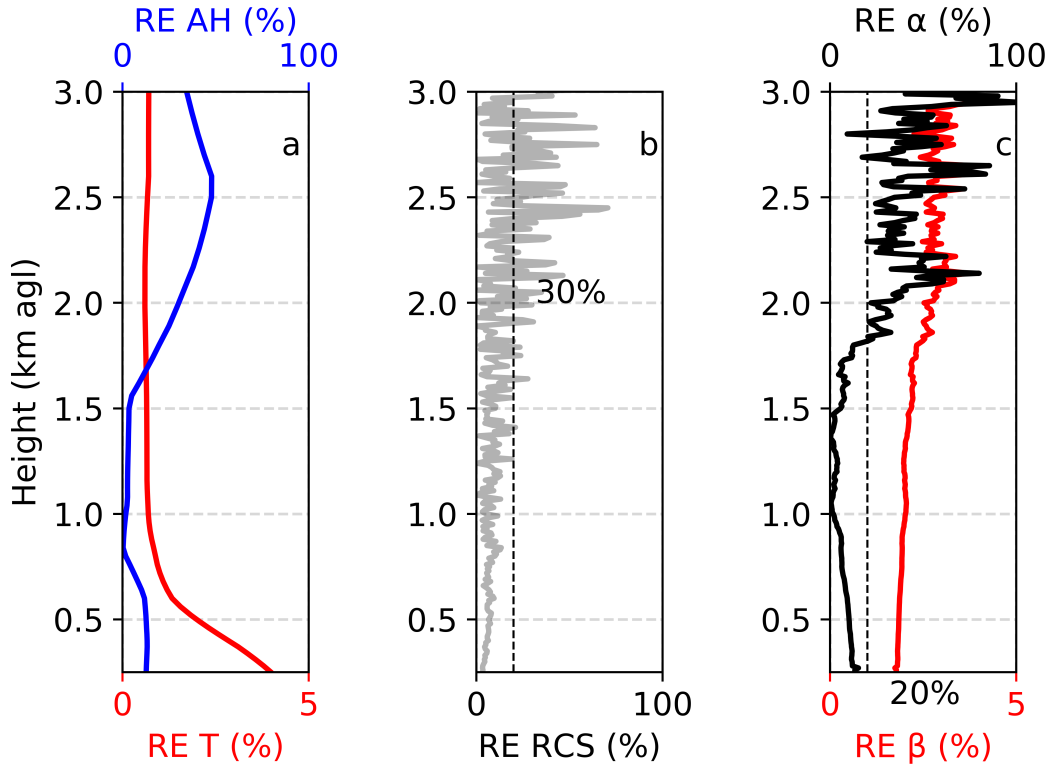


Figure 7: The panel presents the different steps in the example case on 11th October 2019 at 8 UTC for evaluation the relative error (RE) in the inversion process. a) In red lines is represented the temperature and blue line refers to AH, b) is the error committed in the RCS_w signal, and c) RE of the β_p (red line), and α_p (black line)

536 of this error in the Klett inversion is presented in Fig.7c (red line for β_p and
 537 black line for α_p), where RE in the first 2 km agl reached up to 3% in β_p , and
 538 up to 20 % in α_p . The errors in the RCS_w profile due to the use of modelled
 539 data instead of measured are showing that it is imperative the use of accurate
 540 atmospheric profiles for improve the main vaisala product. Additionally, the
 541 RE found here for RCS_w have to be added to the high noise of this product,
 542 which in fact leads to increase the error peaks shown in Fig.7b

543

544 Table2 reports the mean values of the RE in percentage for six cases
 545 evaluated during the two-months study. The cases 1,2,3 were retrieved on
 546 11th October 2019 at 06:00, 09:00, and 12:00 UTC, case 4 to 20th November

Table 2: Mean RE calculated for six inversion cases using the semi-automatic Klett method. The variables evaluated were Temperature, AH, RCS_w , β_p and α_p . The study cases 1,2,3 were measured on 11th October 2019 at 6 h, 9 h, and 12 h respectively, case 4 on 20th November 2019 at 6 h and cases 5 and 6 on 21st November 2019 at 9 h and 12 h. The mean values are calculated for five different atmospheric volumes: from 0 to 0.5 km agl, from 0.5 to 1 km agl, from 1 to 2 km agl

		0 to 0.5 km agl	0.5 to 1 km agl	1 to 2 km agl
T (%)	Case 1	1,8 ± 0,9	0,1 ± 0,1	0,70 ± 0,08
	Case 2	3,9 ± 0,7	1,1 ± 0,3	0,65 ± 0,02
	Case 3	3,4 ± 0,4	2,5 ± 0,4	1,3 ± 0,2
	Case 4	1,5 ± 0,5	0,14 ± 0,08	0,5 ± 0,3
	Case 5	2,1 ± 0,7	0,3 ± 0,1	0,6 ± 0,2
	Case 6	2,0 ± 0,4	1,4 ± 0,3	0,88 ± 0,05
AH(%)	Case 1	10 ± 1	5 ± 3	12 ± 9
	Case 2	13,4 ± 0,9	6 ± 5	7 ± 7
	Case 3	16,5 ± 0,7	11 ± 4	6 ± 4
	Case 4	3 ± 1	6 ± 4	25 ± 13
	Case 5	3 ± 1	18 ± 9	53 ± 17
	Case 6	3 ± 2	20 ± 9	55 ± 17
RCS_w (%)	Case 1	4 ± 10	5 ± 2	8 ± 6
	Case 2	5 ± 9	5 ± 2	8 ± 6
	Case 3	5 ± 5	5 ± 2	9 ± 7
	Case 4	2 ± 3	5 ± 3	7 ± 6
	Case 5	3 ± 4	3 ± 2	7 ± 6
	Case 6	5 ± 9	3 ± 2	8 ± 7
β_p (%)	Case 1	1,81 ± 0,02	1,92 ± 0,04	2,2 ± 0,3
	Case 2	1,77 ± 0,03	1,69 ± 0,02	1,62 ± 0,04
	Case 3	1,67 ± 0,01	1,18 ± 0,02	1,18 ± 0,05
	Case 4	0,85 ± 0,02	0,88 ± 0,03	0,46 ± 0,08
	Case 5	1,26 ± 0,02	1,23 ± 0,07	1,1 ± 0,2
	Case 6	0,96 ± 0,02	0,7 ± 0,2	0,20 ± 0,07
α_p (%)	Case 1	12 ± 1	7 ± 2	10 ± 11
	Case 2	5 ± 1	0,7 ± 0,6	4 ± 2
	Case 3	1,5 ± 0,7	2 ± 1	3 ± 2
	Case 4	3 ± 2	7 ± 3	44 ± 10
	Case 5	1,3 ± 0,8	4 ± 4	18 ± 10
	Case 6	26 ± 3	25 ± 20	73 ± 9

547 2019 at 06:00 UTC and cases 5 and 6 to 21st November 2019 at 09:00 and
548 12:00 UTC. The averages were calculated for 3 different layers for center the
549 attention in the aerosol products: from 0 to 0.5 km agl, from 0.5 to 1 km
550 agl, from 1 to 2 km agl. The inversion products (β_p and α_p) were analyzed
551 until 2 km agl.

552

553 Table2 shows that mean temperature RE were always below 4 % with
554 lower standard deviation (SD). However, in the first 0.5km agl case 2 and
555 3 presented mean values up to 4 %. On the contrary, AH presented higher
556 mean error values mainly above 3 km agl as it was expected from the anal-
557 ysis performed in the previous section with mean errors higher than 40 %
558 (not shown here). Centering the attention in the first two kilometres of the
559 atmosphere, the errors in AH were below 30 %, except for case 5,6 with mean
560 errors up to 55 %. As it was seen on Sec.3, the AH is deeply linked with the
561 transmittance term at correcting the RCS^* signal, therefore the relatively
562 large differences in AH profiles are contributing to RCS_w profiles. Accord-
563 ing to our results, mean RE up to 30 % in AH might cause errors in RCS_w
564 that reach 10 % in the first 2 km agl, and like the amount of water vapor
565 is highly variable in the first two kilometers of the atmosphere, nearly-real
566 measurements of AH will improve the ceilometer signal significantly, other-
567 wise calculations without using real ambient measurements might lead to
568 considerable error increase.

569

570 The retrieved products β_p and α_p have a RE that is influenced firstly by
571 the input profiles which are Rayleigh and RCS_w (including the noises re-
572 mained), and secondly the accurate atmospheric reference to start the back-
573 ward inversion, which is linked with the sunphotometric data for setting the
574 correct LR, among other errors associated to the algorithm calculation itself.
575 From Table2, it is possible to see that in general, the mean RE is lower than
576 3 % below 2 km agl for β_p , meanwhile the errors in α_p can reach 25 % within
577 this height. Some mean errors for α_p in cases 4,5,6 are quite larger than other
578 cases, and this might be linked with the relative elevated AH errors (see on
579 Table2). Considering this error propagation in α_p , we found that without us-
580 ing co-located atmospheric measurements, this inversion product can be also
581 estimated but considering an addition up to 25 % of RE for Vaisala CL51
582 ceilometers, avoiding those cases where AH RE was extremely high. The
583 slight increase in the standard deviation errors reported for the RCS_w in the
584 last air volume evaluated from 1 to 2 km agl (Table2) are associated to the

585 increase of the noise that we already discussed in the pre-processing section,
586 linked with the quality of the ceilometer signals and also in Fig.7b where the
587 RE of the RCS_w increased considerably faster with height, pointing out that
588 aerosol inversion with ceilometers above 3 km agl might lead to larger errors.

589 6. conclusions

590 The purpose of this work is to continue tackling the central problems
591 that Vaisala CL51 ceilometers have for improving aerosol inversion products.
592 Firstly, the ceilometer pre-processing is discussed by taking advantage of
593 the termination hood external tool. Between day and night the instrument
594 presented only small differences in terms of shape and noise levels of DCN
595 signals detected, therefore we decided to work with 30 min-averaged night-
596 time DCN profiles. For the BG analysis, we used a systematic selection of
597 the best height-dependence BG, avoiding that RCS^* goes to negative val-
598 ues within the first 5 km agl. After suppressing DCN and BG, the signal
599 remained positive for more than 5 km agl and S-shape oscillations were min-
600 imized.

601
602 The methodology designed involved the water vapor correction by using
603 a co-located MWR for measuring atmospheric variables. This synergy al-
604 lowed us to improve the quality of the signal by calculating the water vapor
605 transmission term of the lidar equation using measurements of temperature
606 and AH, and deriving from them the N_w . For the inversion, Rayleigh pro-
607 files were calculated using MWR measurements and the RCS_w profiles. In
608 addition, the sun photometer AOD time series were interpolated to 910 nm
609 in order to compare the results with those obtained from the integrated α
610 profiles retrieved after Klett's inversion procedure. For the iterative Klett
611 inversion method, a minimum difference between AOD_{910} and integrated α
612 profiles lower than ≤ 0.001 was set as the condition to constrain the aerosol
613 amount along the iterations.

614
615 An error propagation was performed applying the methodology under
616 two scenarios, considering i) modelled atmospheric data and ii) atmospheric
617 measurements. The error estimation was performed first by means of the
618 RMSE and MBE estimators calculated for two-months of temperature and
619 AH modelled HYSPLIT radiosondes and MWR. The aim was to quantify the
620 error propagation on the two atmospheric variables involved in the RCS_w

621 correction. The errors were calculated for 488 samples covering different at-
622 mospheric scenarios, showing that for temperatures below 2km agl the RMSE
623 is lower than 4 °C, and above is up to 6 °C, whereas AH presented an error
624 up to 2 gm⁻³, which in terms of water vapor correction is significant. The
625 MBE shown that temperature modelled profiles were always underestimating
626 MWR ones (up to -1 °C), and AH MBE was high variable, underestimating
627 the MWR measures from 1 km to 2.3 km agl and from 5.8 km agl to the end
628 of the profile (reaching up -0.5 gm⁻³) and the overestimation reached up 1.5
629 gm⁻³ from ground to 0.2 km agl and from 3 km to 5.8 km agl.

630

631 In summary, we found that the use of modelled data instead atmospheric
632 measurements is primarily influencing the RCS_w , and then the inversion
633 products obtained from the ceilometer. As a result of that, the percentual
634 relative error estimation within the critical zone for aerosol inversion (first
635 2km agl), the temperature presented errors below 4%, while in the first 2 km
636 agl AH were below 25 %. These errors affected the RCS_w signal driving to
637 an error up to 9 % in the first 2km agl. The errors propagated on β_p during
638 Klett calculation were lower than 2.2 %, leading to an error in α_p up to 25
639 %. Therefore, one can conclude that the use of atmospheric modelled data
640 instead of measurements for water vapor correction on vaisala CL51 ceilome-
641 ters will lead large errors on inversion products i.e. α_p .

642

643 Finally, the Klett algorithm could be improved by determining the cal-
644 ibration constant of the instrument tackling one of the E-PROFILE objec-
645 tives. This work can be developed in further studies by having a larger
646 ceilometer database for making a seasonal analysis of the calibration con-
647 stant as function of the internal temperature in a semi-automatic way at
648 ONERA site. In addition, the knowledge of the full overlap height of the
649 system could also help us to improve the inversion products, therefore a fur-
650 ther measurement campaign with ground based lidar operating co-located
651 to the ceilometer might be an ideal solution to have the ceilometer fully
652 characterized.

653 References

- 654 [1] O. Boucher, D. Randall, P. Artaxo, C. Bretherton, G. Feingold,
655 P. Forster, V.-M. Kerminen, Y. Kondo, H. Liao, U. Lohmann, P. Rasch,
656 S. K. Satheesh, S. Sherwood, B. Stevens, X. Y. Zhang, Clouds and

- 657 aerosols, Cambridge University Press, Cambridge, UK, 2013, pp. 571–
658 657. doi:10.1017/CBO9781107415324.016.
- 659 [2] A. Chaikovsky, O. Dubovik, B. Holben, A. Bril, P. Goloub, D. Tanré,
660 G. Pappalardo, U. Wandinger, L. Chaikovskaya, S. Denisov, J. Grudo,
661 A. Lopatin, Y. Karol, T. Lapyonok, V. Amiridis, A. Ansmann, A. Apit-
662 uley, L. Allados-Arboledas, I. Biniotoglou, A. Boselli, G. D’Amico,
663 V. Freudenthaler, D. Giles, M. J. Granados-Muñoz, P. Kokkalis, D. Nico-
664 lae, S. Oshchepkov, A. Papayannis, M. R. Perrone, A. Pietruczuk,
665 F. Rocadenbosch, M. Sicard, I. Slutsker, C. Talianu, F. DeÂ Tomasi,
666 A. Tsekeri, J. Wagner, X. Wang, Lidar-radiometer inversion code
667 (liric) for the retrieval of vertical aerosol properties from com-
668 bined lidar/radiometer data: development and distribution in ear-
669 linet, *Atmospheric Measurement Techniques* 9 (2016) 1181–1205. URL:
670 <https://www.atmos-meas-tech.net/9/1181/2016/>. doi:10.5194/amt-
671 9-1181-2016.
- 672 [3] A. Lopatin, O. Dubovik, A. Chaikovsky, P. Goloub, T. Lapyonok,
673 D. Tanré, P. Litvinov, Enhancement of aerosol characterization us-
674 ing synergy of lidar and sun-photometer coincident observations: the
675 garrlic algorithm, *Atmospheric Measurement Techniques* 6 (2013)
676 2065–2088. URL: <https://www.atmos-meas-tech.net/6/2065/2013/>.
677 doi:10.5194/amt-6-2065-2013.
- 678 [4] J. A. Benavent-Oltra, R. Román, M. J. Granados-Muñoz,
679 D. Pérez-Ramírez, P. Ortiz-Amezcuca, C. Denjean, A. Lopatin,
680 H. Lyamani, B. Torres, J. L. Guerrero-Rascado, D. Fuertes,
681 O. Dubovik, A. Chaikovsky, F. J. Olmo, M. Mallet, L. Alados-
682 Arboledas, Comparative assessment of grasp algorithm for a
683 dust event over granada (spain) during charmex-adrimed 2013
684 campaign, *Atmospheric Measurement Techniques* 10 (2017) 4439–
685 4457. URL: <https://www.atmos-meas-tech.net/10/4439/2017/>.
686 doi:10.5194/amt-10-4439-2017.
- 687 [5] J. A. Benavent-Oltra, R. Román, J. A. Casquero-Vera, D. Pérez-
688 Ramírez, H. Lyamani, P. Ortiz-Amezcuca, A. E. Bedoya-Velásquez,
689 G. de Arruda Moreira, A. Barreto, A. Lopatin, D. Fuertes, M. Her-
690 rera, B. Torres, O. Dubovik, J. L. Guerrero-Rascado, P. Goloub,
691 F. J. Olmo-Reyes, L. Alados-Arboledas, Different strategies to

- 692 retrieve aerosol properties at night-time with the grasp algo-
693 rithm, *Atmospheric Chemistry and Physics* 19 (2019) 14149–
694 14171. URL: <https://www.atmos-chem-phys.net/19/14149/2019/>.
695 doi:10.5194/acp-19-14149-2019.
- 696 [6] A. E. Bedoya-Velásquez, F. Navas-Guzmán, M. J. Granados-Muñoz,
697 G. Titos, R. Román, J. A. Casquero-Vera, P. Ortiz-Amezcuca, J. A.
698 Benavent-Oltra, G. de Arruda Moreira, E. Montilla-Rosero, C. D. Hoyos,
699 B. Artiñano, E. Coz, F. J. Olmo-Reyes, L. Alados-Arboledas, J. L.
700 Guerrero-Rascado, Hygroscopic growth study in the framework of ear-
701 linet during the slope i campaign: synergy of remote sensing and in situ
702 instrumentation, *Atmospheric Chemistry and Physics* 18 (2018) 7001–
703 7017. URL: <https://www.atmos-chem-phys.net/18/7001/2018/>.
704 doi:10.5194/acp-18-7001-2018.
- 705 [7] G. de Arruda Moreira, J. L. Guerrero-Rascado, J. A. Benavent-
706 Oltra, P. Ortiz-Amezcuca, R. Román, A. E. Bedoya-Velásquez, J. A.
707 Bravo-Aranda, F. J. Olmo Reyes, E. Landulfo, L. Alados-Arboledas,
708 Analyzing the turbulent planetary boundary layer by remote sensing
709 systems: the doppler wind lidar, aerosol elastic lidar and microwave
710 radiometer, *Atmospheric Chemistry and Physics* 19 (2019) 1263–
711 1280. URL: <https://www.atmos-chem-phys.net/19/1263/2019/>.
712 doi:10.5194/acp-19-1263-2019.
- 713 [8] A. E. Bedoya-Velásquez, G. Titos, J. A. Bravo-Aranda, M. Haeffe-
714 lin, O. Favez, J.-E. Petit, J. A. Casquero-Vera, F. J. Olmo-Reyes,
715 E. Montilla-Rosero, C. D. Hoyos, L. Alados-Arboledas, J. L. Guerrero-
716 Rascado, Long-term aerosol optical hygroscopicity study at the
717 actris sirta observatory: synergy between ceilometer and in situ
718 measurements, *Atmospheric Chemistry and Physics* 19 (2019) 7883–
719 7896. URL: <https://www.atmos-chem-phys.net/19/7883/2019/>.
720 doi:10.5194/acp-19-7883-2019.
- 721 [9] M. Haeffelin, Q. Laffineur, J.-A. Bravo-Aranda, M.-A. Drouin, J.-
722 A. Casquero-Vera, J.-C. Dupont, H. De Backer, Radiation fog for-
723 mation alerts using attenuated backscatter power from automatic li-
724 dars and ceilometers, *Atmospheric Measurement Techniques* 9 (2016)
725 5347–5365. URL: <https://www.atmos-meas-tech.net/9/5347/2016/>.
726 doi:10.5194/amt-9-5347-2016.

- 727 [10] M. Wiegner, F. Madonna, I. Biniotoglou, R. Forkel, J. Gasteiger,
728 A. Geiß, G. Pappalardo, K. Schäfer, W. Thomas, What is the ben-
729 efit of ceilometers for aerosol remote sensing? an answer from ear-
730 linet, *Atmospheric Measurement Techniques* 7 (2014) 1979–1997. URL:
731 <https://www.atmos-meas-tech.net/7/1979/2014/>. doi:10.5194/amt-
732 7-1979-2014.
- 733 [11] Y. Jin, K. Kai, K. Kawai, T. Nagai, T. Sakai, A. Yamazaki,
734 A. Uchiyama, D. Batdorj, N. Sugimoto, T. Nishizawa, Ceilometer
735 calibration for retrieval of aerosol optical properties, *Journal of Quan-
736 titative Spectroscopy and Radiative Transfer* 153 (2015) 49 – 56. URL:
737 <http://www.sciencedirect.com/science/article/pii/S0022407314004257>.
738 doi:<https://doi.org/10.1016/j.jqsrt.2014.10.009>, topical issue on optical
739 particle characterization and remote sensing of the atmosphere: Part
740 II.
- 741 [12] A. Cazorla, J. A. Casquero-Vera, R. Román, J. L. Guerrero-Rascado,
742 C. Toledano, V. E. Cachorro, J. A. G. Orza, M. L. Cancillo, A. Serrano,
743 G. Titos, M. Pandolfi, A. Alastuey, N. Hanrieder, L. Alados-Arboledas,
744 Near-real-time processing of a ceilometer network assisted with sun-
745 photometer data: monitoring a dust outbreak
746 over the iberian peninsula, *Atmospheric Chem-
747 istry and Physics* 17 (2017) 11861–11876. URL:
748 <https://www.atmos-chem-phys.net/17/11861/2017/>.
749 doi:10.5194/acp-17-11861-2017.
- 750 [13] R. Román, J. Benavent-Oltra, J. Casquero-Vera, A. Lopatin, A. Ca-
751 zorla, H. Lyamani, C. Denjean, D. Fuertes, D. Pérez-Ramírez,
752 B. Torres, C. Toledano, O. Dubovik, V. Cachorro, A. [de Fru-
753 to], F. Olmo, L. Alados-Arboledas, Retrieval of aerosol pro-
754 files combining sunphotometer and ceilometer measurements in
755 grasp code, *Atmospheric Research* 204 (2018) 161 – 177. URL:
756 <http://www.sciencedirect.com/science/article/pii/S0169809517312577>.
757 doi:<https://doi.org/10.1016/j.atmosres.2018.01.021>.
- 758 [14] M. Herreras, R. Román, A. Cazorla, C. Toledano, H. Lyamani,
759 B. Torres, V. Cachorro, F. Olmo, L. Alados-Arboledas, A. de Fru-
760 to, Evaluation of retrieved aerosol extinction profiles using

- 761 as reference the aerosol optical depth differences between var-
762 ious heights, *Atmospheric Research* 230 (2019) 104625. URL:
763 <https://www.sciencedirect.com/science/article/pii/S0169809519300432>.
764 doi:10.1016/j.atmosres.2019.1046259.
- 765 [15] G. Titos, M. Ealo, R. Román, A. Cazorla, Y. Sola, O. Dubovik,
766 A. Alastuey, M. Pandolfi, Retrieval of aerosol properties from
767 ceilometer and photometer measurements: long-term evaluation
768 with in situ data and statistical analysis at montsec (southern
769 pyrenees), *Atmospheric Measurement Techniques* 12 (2019) 3255–
770 3267. URL: <https://www.atmos-meas-tech.net/12/3255/2019/>.
771 doi:10.5194/amt-12-3255-2019.
- 772 [16] S. Kotthaus, E. O’Connor, C. Münkler, C. Charlton-Perez, M. Haeffelin,
773 A. M. Gabey, C. S. B. Grimmond, Recommendations for processing
774 atmospheric attenuated backscatter profiles from vaisala cl31 ceilome-
775 ters, *Atmospheric Measurement Techniques* 9 (2016) 3769–3791. URL:
776 <https://www.atmos-meas-tech.net/9/3769/2016/>. doi:10.5194/amt-
777 9-3769-2016.
- 778 [17] C. R. Marcos, J. L. Gómez-Amo, C. Peris, R. Pedrós, M. P.
779 Utrillas, J. A. Martínez-Lozano, Analysis of four years of ceilometer-
780 derived aerosol backscatter profiles in a coastal site of the western
781 mediterranean, *Atmospheric Research* 213 (2018) 331 – 345. URL:
782 <http://www.sciencedirect.com/science/article/pii/S016980951830468X>.
783 doi:<https://doi.org/10.1016/j.atmosres.2018.06.016>.
- 784 [18] M. Wiegner, J. Gasteiger, Correction of water vapor ab-
785 sorption for aerosol remote sensing with ceilometers, *At-
786 mospheric Measurement Techniques* 8 (2015) 3971–3984. URL:
787 <https://www.atmos-meas-tech.net/8/3971/2015/>. doi:10.5194/amt-
788 8-3971-2015.
- 789 [19] J. D. Klett, Lidar inversion with variable backscat-
790 ter/extinction ratios, *Appl. Opt.* 24 (1985) 1638–1643.
791 URL: <http://ao.osa.org/abstract.cfm?URI=ao-24-11-1638>.
792 doi:10.1364/AO.24.001638.
- 793 [20] J. D. Klett, Stable analytical inversion solution for pro-
794 cessing lidar returns, *Appl. Opt.* 20 (1981) 211–220.

- 795 URL: <http://ao.osa.org/abstract.cfm?URI=ao-20-2-211>.
796 doi:10.1364/AO.20.000211.
- 797 [21] T. Rose, S. Crewell, U. Löhnert, C. Simmer, A network suitable
798 microwave radiometer for operational monitoring of the cloudy
799 atmosphere, *Atmospheric Research* 75 (2005) 183 – 200. URL:
800 <http://www.sciencedirect.com/science/article/pii/S0169809505000189>.
801 doi:<https://doi.org/10.1016/j.atmosres.2004.12.005>, cLIWA-NET: Ob-
802 servation and Modelling of Liquid Water Clouds.
- 803 [22] A. E. Bedoya-Velásquez, F. Navas-Guzmán, G. de Arruda Moreira,
804 R. Román, A. Cazorla, P. Ortiz-Amezcuá, J. A. Benavent-Oltra,
805 L. Alados-Arboledas, F. J. Olmo-Reyes, I. Foyo-Moreno, E. Montilla-
806 Rosero, C. D. Hoyos, J. L. Guerrero-Rascado, Seasonal analysis
807 of the atmosphere during five years by using microwave radiometry
808 over a mid-latitude site, *Atmospheric Research* 218 (2019) 78 – 89. URL:
809 <http://www.sciencedirect.com/science/article/pii/S0169809518312857>.
810 doi:<https://doi.org/10.1016/j.atmosres.2018.11.014>.
- 811 [23] B. Holben, T. Eck, I. Slutsker, D. Tanré, J. Buis, A. Set-
812 zer, E. Vermote, J. Reagan, Y. Kaufman, T. Nakajima,
813 F. Lavenu, I. Jankowiak, A. Smirnov, Aeronet—a federated
814 instrument network and data archive for aerosol characteriza-
815 tion, *Remote Sensing of Environment* 66 (1998) 1 – 16. URL:
816 <http://www.sciencedirect.com/science/article/pii/S0034425798000315>.
817 doi:[https://doi.org/10.1016/S0034-4257\(98\)00031-5](https://doi.org/10.1016/S0034-4257(98)00031-5).
- 818 [24] O. Dubovik, M. D. King, A flexible inversion algo-
819 rithm for retrieval of aerosol optical properties from sun
820 and sky radiance measurements, *Journal of Geophys-
821 ical Research: Atmospheres* 105 (2000) 20673–20696. URL:
822 <https://agupubs.onlinelibrary.wiley.com/doi/abs/10.1029/2000JD900282>.
823 doi:10.1029/2000JD900282.
- 824 [25] O. Dubovik, B. Holben, T. F. Eck, A. Smirnov, Y. J. Kaufman,
825 M. D. King, D. Tanré, I. Slutsker, Variability of absorption and
826 optical properties of key aerosol types observed in worldwide loca-
827 tions, *Journal of the Atmospheric Sciences* 59 (2002) 590–608. URL:
828 [https://doi.org/10.1175/1520-0469\(2002\)059<0590:VOAOP>2.0.CO;2](https://doi.org/10.1175/1520-0469(2002)059<0590:VOAOP>2.0.CO;2).
829 doi:10.1175/1520-0469(2002)059;0590:VOAOP;2.0.CO;2.

- 830 [26] O. Dubovik, A. Sinyuk, T. Lapyonok, B. N. Holben, M. Mishchenko,
831 P. Yang, T. F. Eck, H. Volten, O. Muñoz, B. Veihelmann,
832 W. J. van der Zande, J.-F. Leon, M. Sorokin, I. Slutsker,
833 Application of spheroid models to account for aerosol particle
834 nonsphericity in remote sensing of desert dust, *Journal of Geophysical Research: Atmospheres* 111 (2006). URL:
835 <https://agupubs.onlinelibrary.wiley.com/doi/abs/10.1029/2005JD006619>.
836 doi:10.1029/2005JD006619.
837
- 838 [27] D. M. Giles, A. Sinyuk, M. G. Sorokin, J. S. Schafer, A. Smirnov,
839 I. Slutsker, T. F. Eck, B. N. Holben, J. R. Lewis, J. R. Campbell,
840 E. J. Welton, S. V. Korkin, A. I. Lyapustin, *Advancements in the aerosol robotic network (aeronet) version 3 database – automated near-real-time quality control algorithm with improved cloud screening for sun photometer aerosol optical depth (aod) measurements*, *Atmospheric Measurement Techniques* 12 (2019) 169–209. URL:
841 <https://www.atmos-meas-tech.net/12/169/2019/>. doi:10.5194/amt-12-169-2019.
842
843
844
845
846
- 847 [28] A. F. Stein, R. R. Draxler, G. D. Rolph, B. J. B. Stunder,
848 M. D. Cohen, F. Ngan, *Noaa’s hysplit atmospheric transport and dispersion modeling system*, *Bulletin of the American Meteorological Society* 96 (2015) 2059–2077. URL:
849 <https://doi.org/10.1175/BAMS-D-14-00110.1>. doi:10.1175/BAMS-
850 D-14-00110.1. arXiv:<https://doi.org/10.1175/BAMS-D-14-00110.1>.
851
852